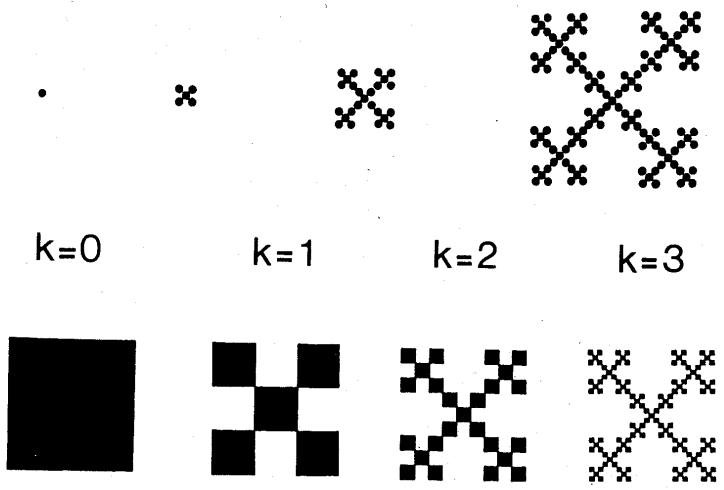

Figure 2.1. Example for the construction of a deterministic fractal embedded into two dimensions. Figure 2.1a demonstrates how one can generate a growing fractal using an iteration procedure. In Fig. 2.1b an analogous structure is constructed by subsequent divisions of the original square. Both procedures lead to fractals for $k \to \infty$ with the same dimension $D \simeq 1.465$.

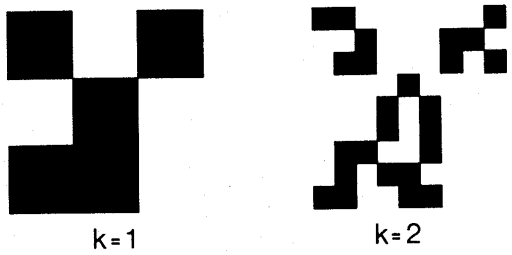

Figure 2.2. Construction of a stochastic fractal. Its fractal dimension is exactly the same as that of the structure shown in Fig. 2.1, despite the fact that they look quite different.

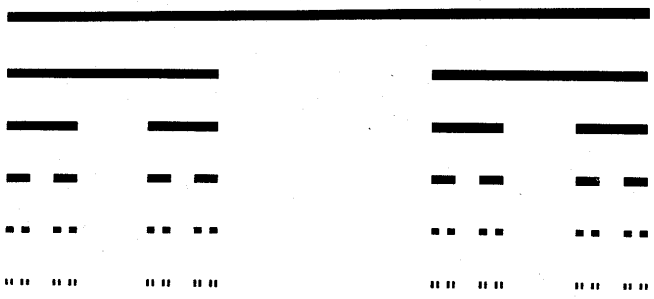

Figure 2.3. The triadic Cantor set shown in this figure is generated on the unit interval by replacing each of the intervals obtained at a given stage with two shorter ones.

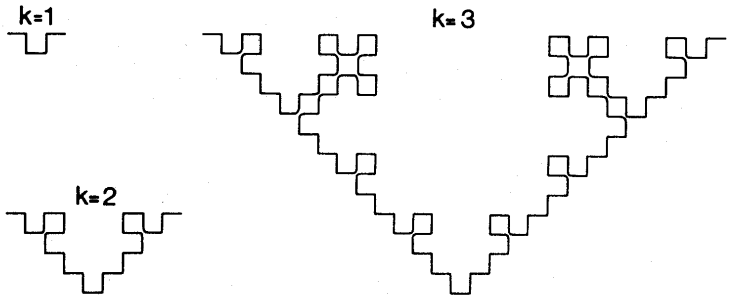

Figure 2.4. Construction of a growing fractal curve having the same fractal dimension as the objects shown in Figs. 2.1 and 2.2.

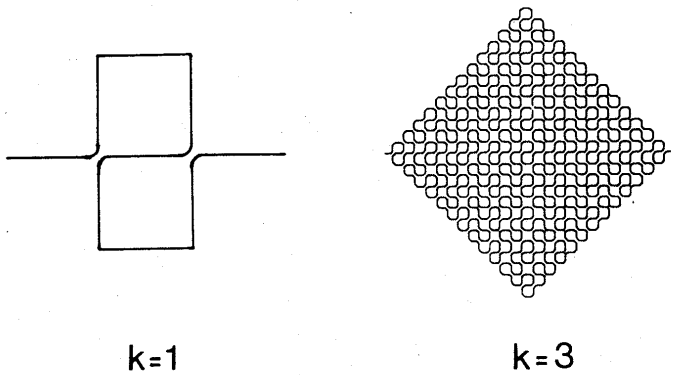

Figure 2.5. Application of Eq. (2.10) to the above displayed Peano curve gives $D = d = 2$ which means that this construction does not lead to a fractal according to the definition given in Section 2.2.

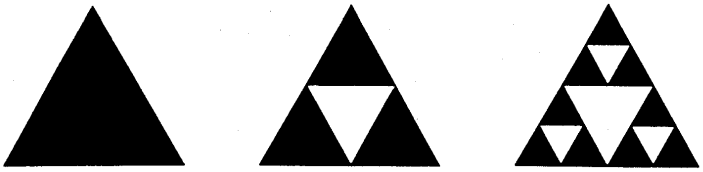

Figure 2.6. The Sierpinski gasket shown in this figure has loops on all length scales.

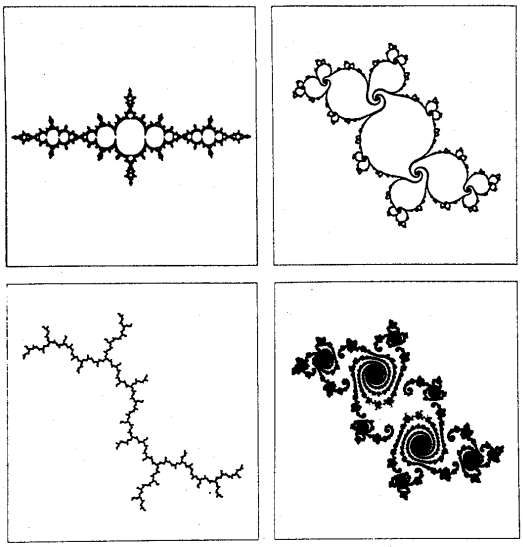

Figure 2.7. The rich variety of apparently self-similar Julia sets is well demonstrated by the above selected examples reproduced from Peitgen and Richter (1986).

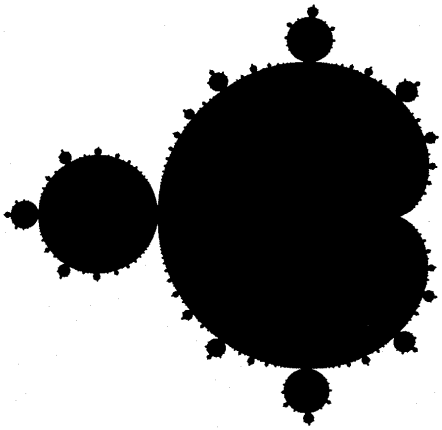

Figure 2.8. The region of μ values (Mandelbrot set) for which the iterates given by (2.20) remain finite for arbritrary k (Mandelbrot 1982).

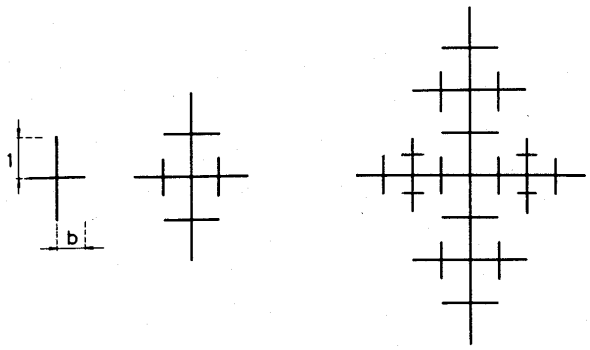

Figure 2.9. This non-uniform fractal grows by adding to the four principal tips of the $(n-1)$th configuration the structure itself without the lower main stem. This addition has to be done by applying appropriate rotation and shrinking to keep the ratio of the corresponding branches equal to $b < 1$.

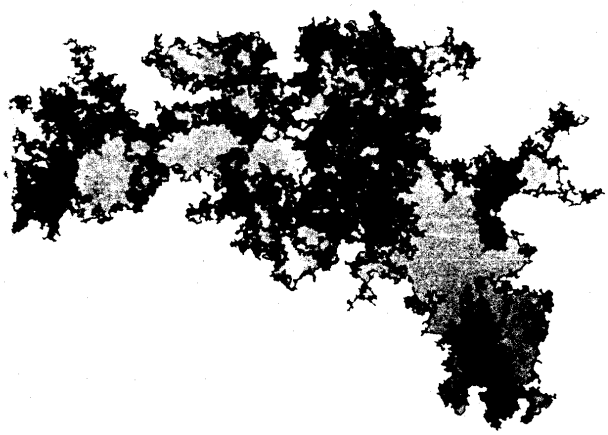

Figure 2.10. Example for a random coastline. This Brown hull represents the external perimeter of the trajectory of a looping random walk on the plane which is indicated by a darker line (Mandelbrot 1982).

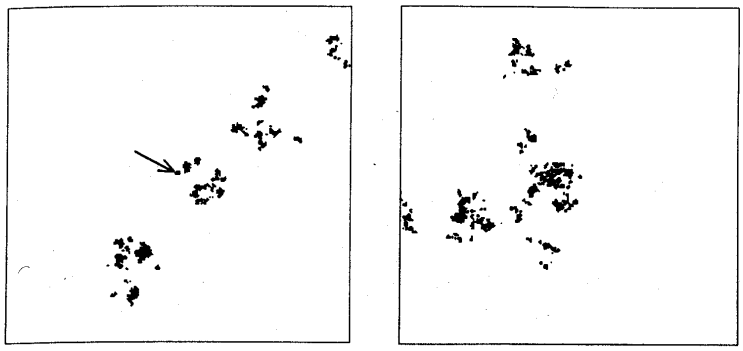

Figure 2.11. The shapes of disconnected clusters corresponding to the stopovers of a long Levy flight on the plane. The stochastic self-similarity of the clusters is demonstrated by blowing up small parts of the configurations. The picture on the right side is an approximately 100 times enlarged image of a tiny region in the left configuration indicated by the arrow (Mandelbrot 1982).

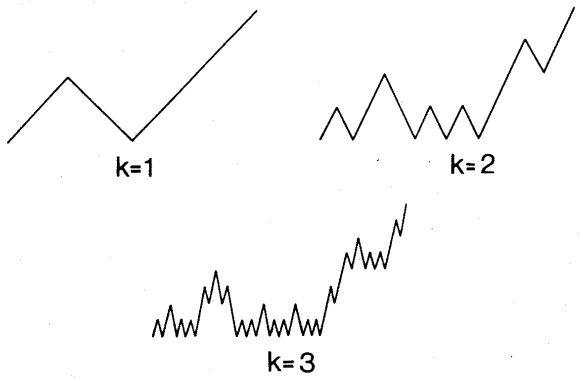

Figure 2.12. Deterministic model for a self-affine function defined on the unit interval. The single-valued character of the function is preserved by an appropriate distortion of the z-shaped generator ($k = 1$) of the structure.

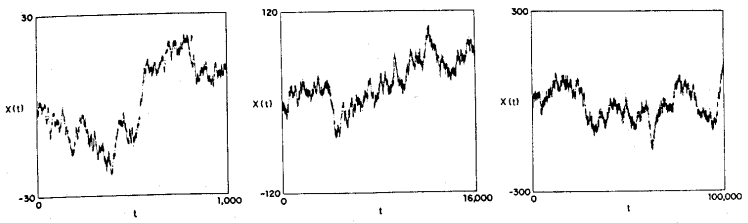

Figure 2.13. These plots of $X_{1/2}(t)$ were obtained by rescaling of Brownian plots of various lengths. For each of the three plots the vertical scale is proportional to the square root of the horizontal scale (Meakin 1986).

Figure 2.14. A Brownian surface having a local fractal dimension close to 2.4 (Mandelbrot 1982).

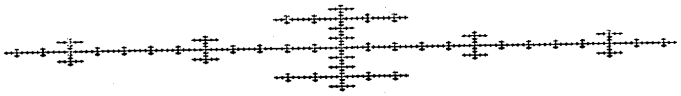

Figure 2.15. This growing self-affine fractal is generated by a procedure analogous to that used for constructing Fig. 2.1a, except that in the present case the seed configuration is not isotropic (Jullien and Botet 1987).

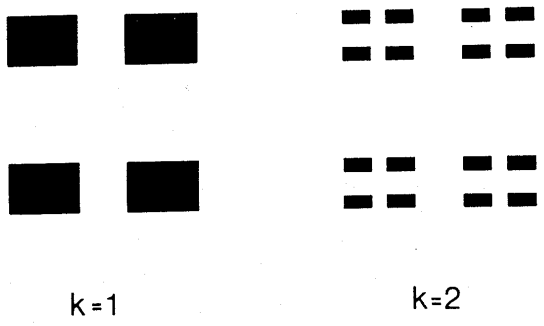

Figure 2.16. Generating a disconnected self-affine fractal embedded into two dimensions using elongated rectangles instead of squares during its construction.

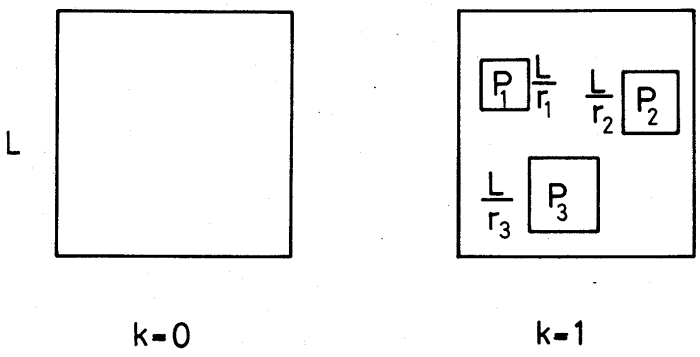

Figure 3.1. Construction of a fractal measure defined on a non-uniform fractal support embedded into two dimensions. The multifractal is obtained after infinitely many recursions.

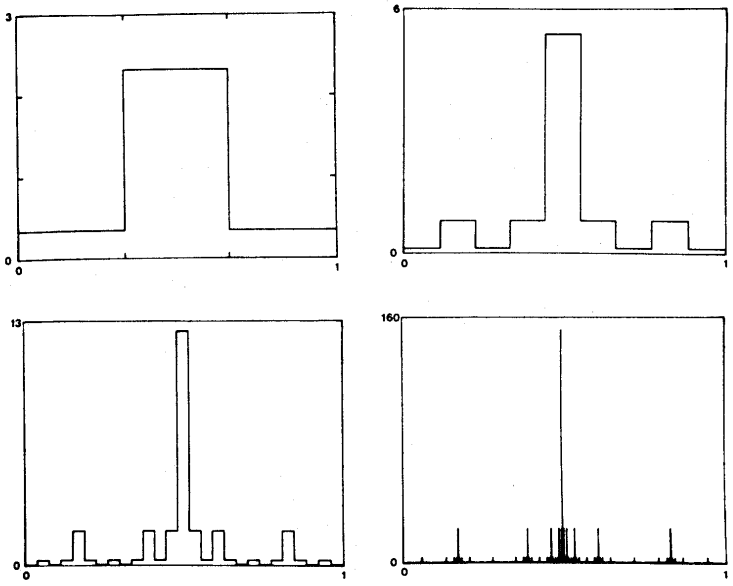

Figure 3.2. The first steps of constructing a fractal measure on the unit interval (Farmer 1982).

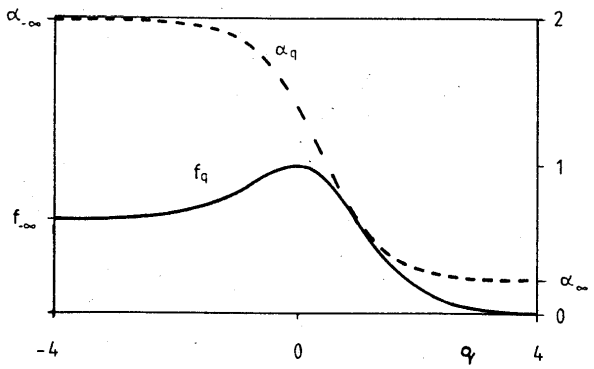

Figure 3.3. The q-dependence of the fractal dimension f_q and the exponent α_q for the multifractal shown in Fig. 3.2 (Tél 1988).

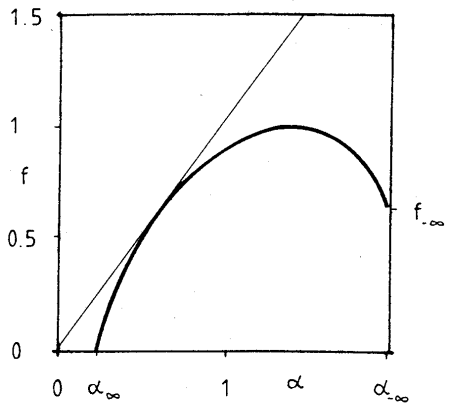

Figure 3.4. The $f(\alpha)$ spectrum of fractal dimensionalities for the multifractal of Fig. 3.2. The straight line corresponds to $f = \alpha$ (Tél 1988).

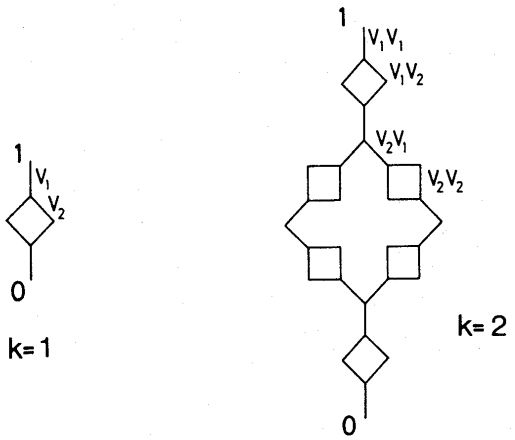

Figure 3.5. Fractal model for hierarchical networks of resistors. The distribution of voltage drops exhibits multifractal scaling.

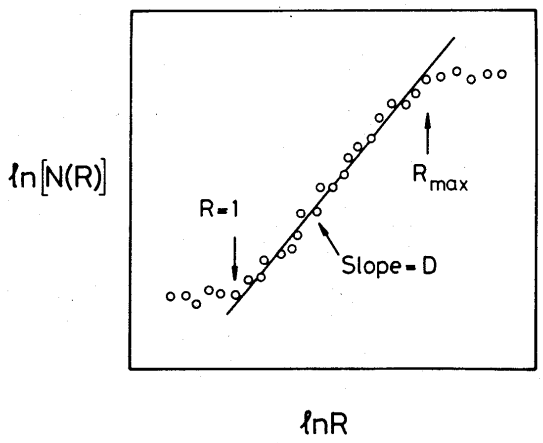

Figure 4.4. Schematic log-log plot of the numerically determined number of particles $N(R)$ belonging to a fractal and being within a sphere of radius R. If R is smaller than the particle size or larger than the linear size of the structure a trivial behaviour is observed. The fractal dimension is obtained by fitting a straight line to the data in the scaling region.

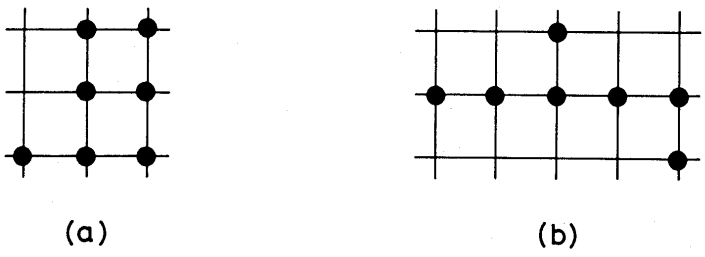

Figure 5.1. Two possible configurations (clusters) consisting of the same number of particles (black sites). The statistical weight of a given cluster depends on its geometry. For example, the probability associated with configuration (a) is larger for a growth process which preferably produces compact clusters.

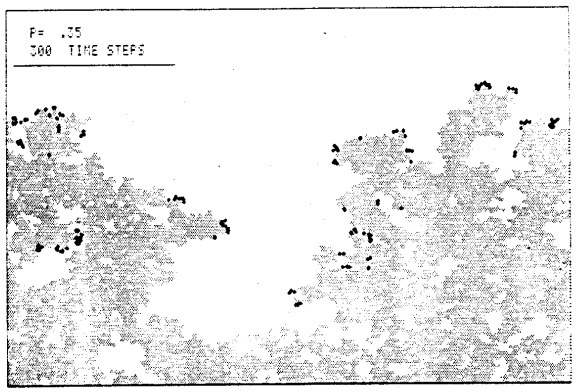

Figure 5.2. Result of a typical run of growing a percolation cluster along a line for $p = p_c$. The cluster is generated on a triangular lattice by adding to it all of the growth sites at each time step. The growth sites are denoted by heavy dots. (Grassberger 1985).

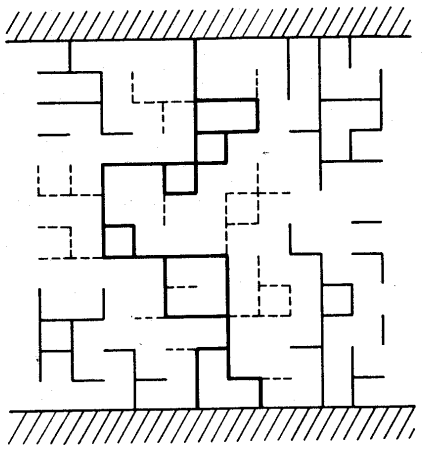

Figure 5.5. Schematic picture of the backbone of a percolation cluster. The bonds belonging to the backbone are drawn with heavy lines, while the bonds leading to deadends are denoted by dashed lines.

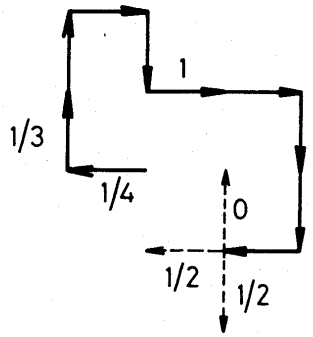

Figure 5.7. Example for a short IGSAW on the square lattice. To recognize whether the next step would lead to a trap it is enough to know the local configuration and the direction of the old part.

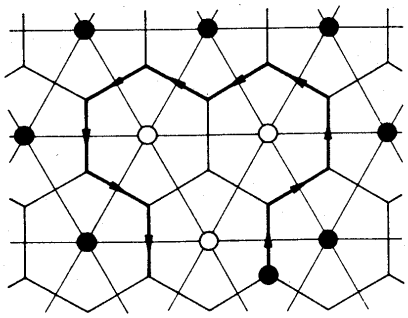

Figure 5.8. Example for a short IGSAW on the hexagonal lattice. It follows the perimeter of a site percolation cluster on the dual triangular lattice.

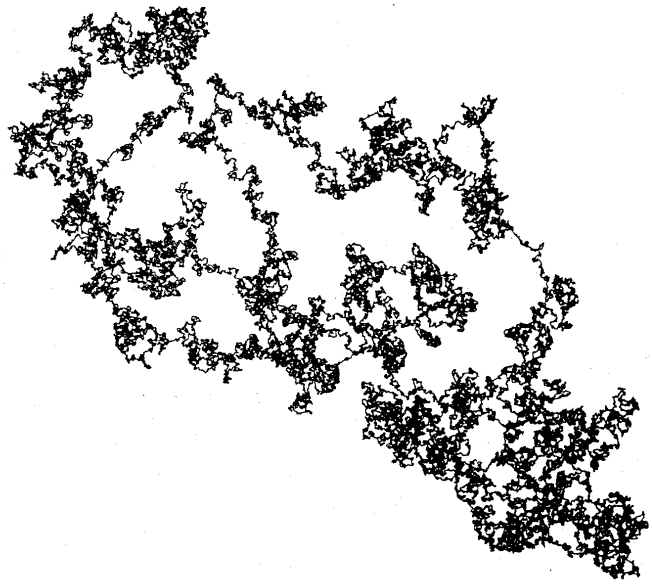

Figure 5.9. External perimeter of a percolation cluster generated by the ring-forming version of IGSAW on the square lattice. This configuration contains 194 468 sites (Ziff 1986).

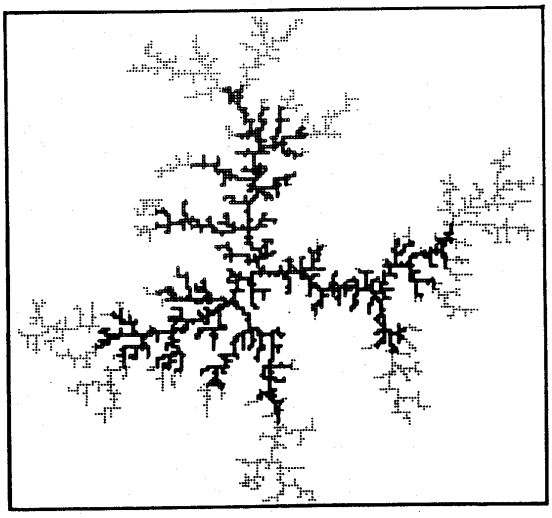

Figure 6.1. A relatively small DLA cluster consisting of 3000 particles. To demonstrate the screening effect the first 1500 particles attached to the aggregate are open circles, while the rest are dots (Witten and Sander 1983).

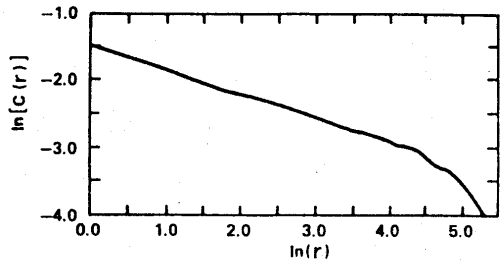

Figure 6.2. Double logarithmic plot of the density-density correlation function $c(r)$ (2.14) for a DLA cluster of 11260 particles generated on the square lattice (Meakin 1983a).

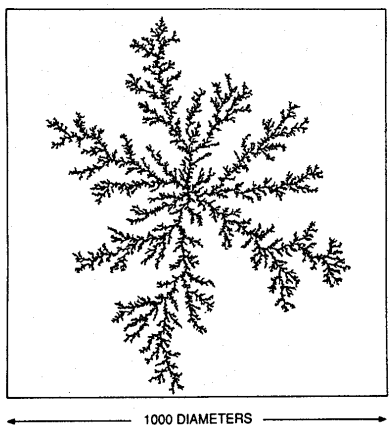

Figure 6.3. A typical off-lattice DLA cluster of 50,000 particles. A comparison with Fig. 6.1 showing a much smaller aggregate illustrates the stochastic self-similarity of diffusion-limited aggregates (Meakin 1985b).

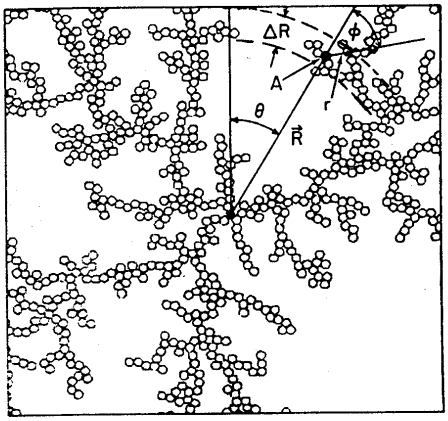

Figure 6.5. Central part of an off-lattice DLA cluster. The tangential correlations as a function of the angle θ are determined in a layer of width δR being at a distance R from the centre (Meakin and Vicsek 1985).

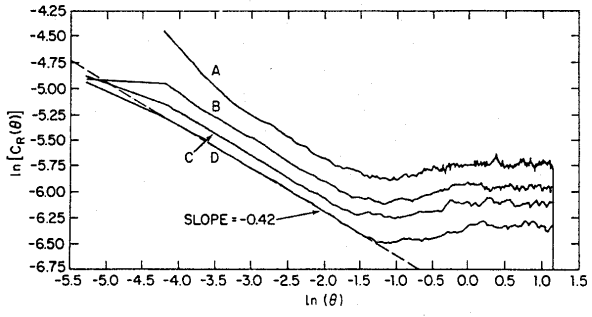

Figure 6.6. Tangential correlations in off-lattice DLA clusters of 50,000 particles. The results were obtained by averaging over the interval $\delta R = R \pm 0.05R$, where for the curves $A - D$ the radius R was respectively equal to 75, 150, 225 and 300 (Meakin and Vicsek 1985).

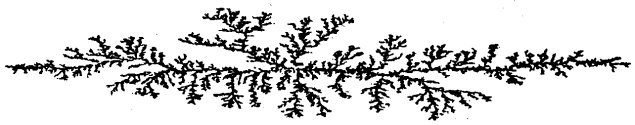

Figure 6.7. A representative DLA cluster grown using anisotropic sticking probability (Ball *et al* 1985).

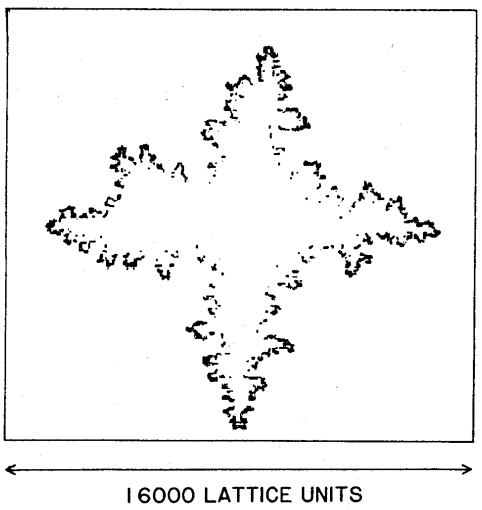

Figure 6.8. Envelope of a very large DLA cluster (consisting of 4×10^6 particles) generated on the square lattice. The effect of the lattice anisotropy is shown by plotting the last 2×10^5 particles attached to the cluster (Meakin *et al* 1987).

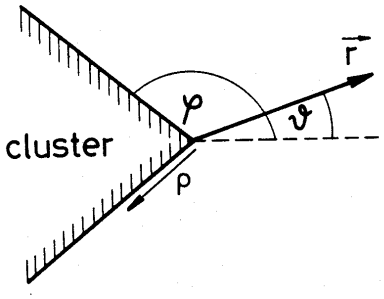

Figure 6.9. Modelling the region around the tips of DLA clusters with a cone of exterior half angle φ.

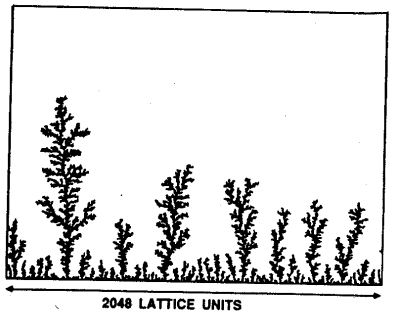

Figure 6.15. Forest of clusters grown on the square lattice along a 300 lattice unit long straight substrate. Because of screening, diffusion-limited deposition leads to a power law distribution of tree sizes (Meakin 1983b).

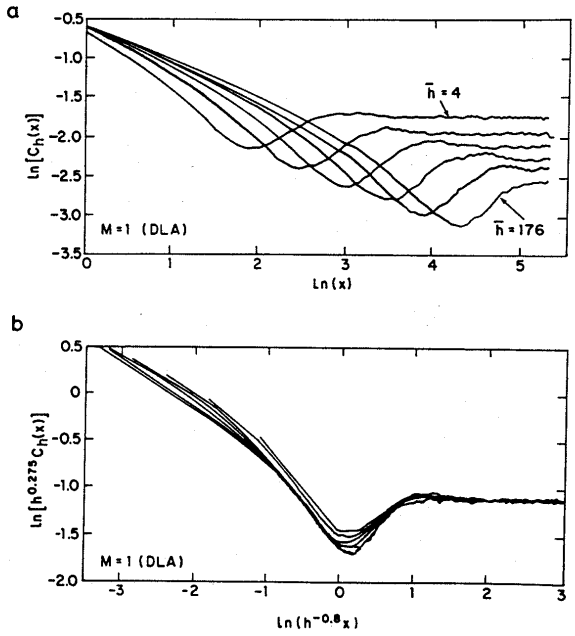

Figure 6.16. (a) Density correlations $c_h(x)$ in the lateral (x) direction within a layer of a two-dimensional deposit being at a distance h from the substrate. (b) The data for various h are shown to collapse into a single curve using the scaling form 6.41 (Meakin *et al* 1988).

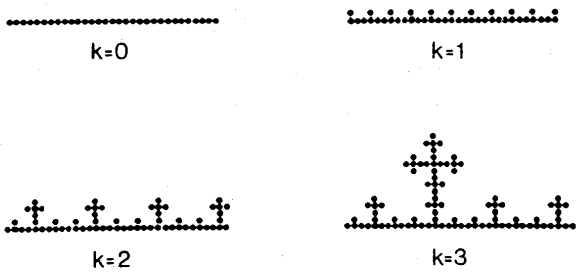

Figure 6.17. Deterministic fractal model for diffusion-limited deposition (Vicsek 1983).

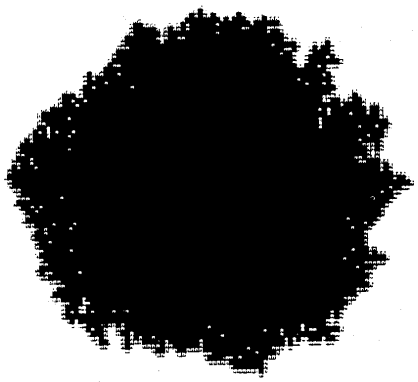

Figure 7.1. This Eden cluster consisting of 5000 particles was grown from a single seed by occupying randomly selected perimeter sites (version A).

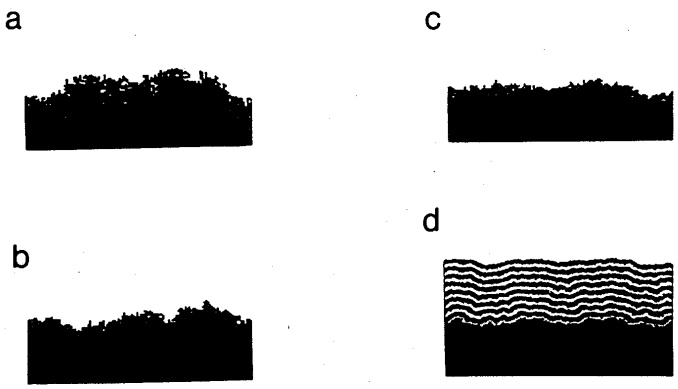

Figure 7.2. Eden deposits of 25000 particles generated on a substrate of width $L = 160$ using the noise reduction algorithm with $m = 1, 2, 4$ (a–c). Figure 7.2d shows the time evolution of a cluster for which at $N = 10000$ noise reduction with $m = 16$ was switched on (following a growth with $m = 1$) (Kertész and Wolf 1988).

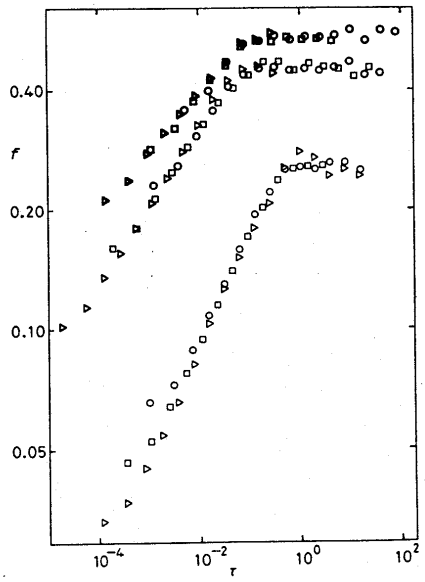

Figure 7.3. Scaling plot for $d = 2$ (lower curve, $L = 60$ (○), 120 (□), and 240 (▷)), for $d = 3$ (middle curve, $L_1 \times L_2 = 10 \times 10$ (○), 30×32 (□) and 120×128 (▷)), and for $d = 4$ (upper curve, $L_1 \times L_2 \times L_3 = 4 \times 4 \times 4$ (○), $9 \times 10 \times 10$ (□), and $30 \times 32 \times 32$ (▷)). The noise-reduction parameter is $m = 8$ for all data (Wolf and Kertész 1987b).

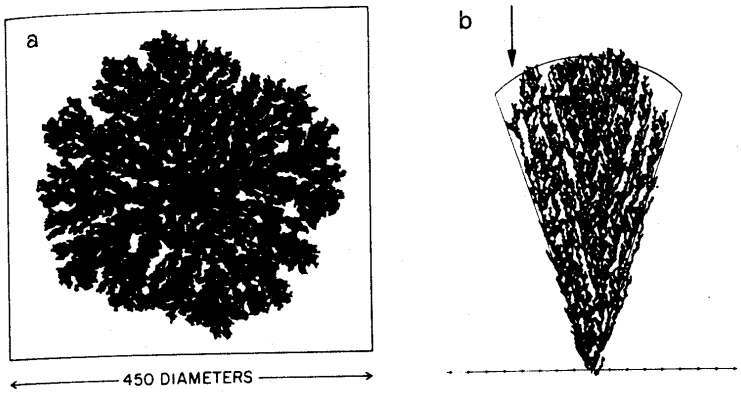

Figure 7.4. Off-lattice ballistic aggregates. (a) This cluster consisting of 180,000 particles was generated by simulating randomly oriented trajectories (Meakin 1985b). (b) Randomly positioned vertical trajectories lead to a fan-like structure when a single seed particle is used (Ramanlal and Sander 1985).

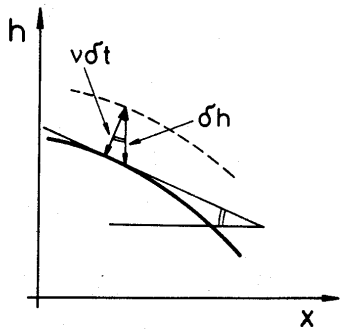

Figure 7.7. Schematic picture showing the increment of h as the growth locally occurs along the normal to the interface.

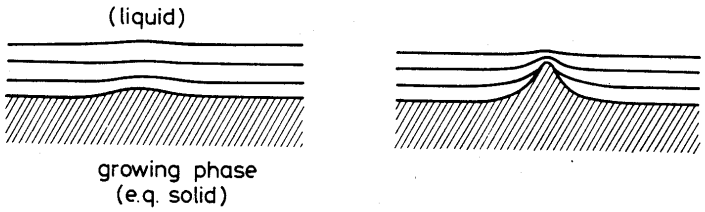

Figure 9.1. Schematic illustration of the Mullins-Sekerka instability. The function u (e.g., the temperature) is the same along the lines drawn close to the interface.

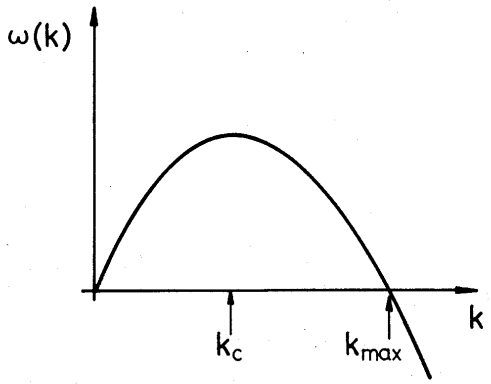

Figure 9.2. Schematic representation of the dispersion relation (9.5). Deformations with a characteristic wave number k for which $\omega > 0$ grow in an unstable manner, while the region $\omega < 0$ corresponds to a stable regime.

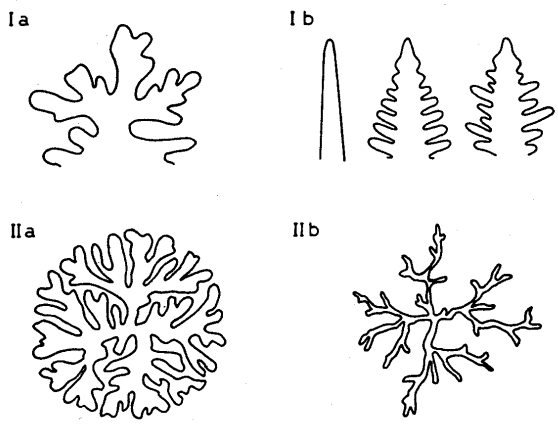

Figure 9.3. Schematic pictures of the major types of patterns which typically occur during unstable interfacial growth.

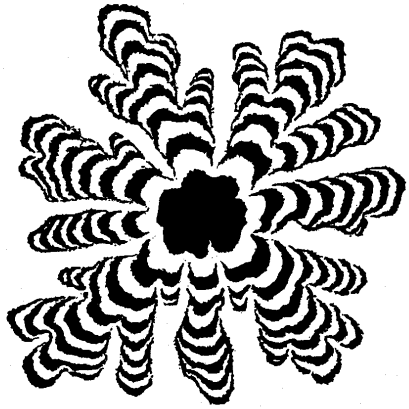

Figure 9.6. Various stages in the growth of an off-lattice cluster generated using a curvature-dependent sticking probability. This figure illustrates the crossover from a compact to a fractal structure as the aggregate grows larger (Meakin *et al* 1987).

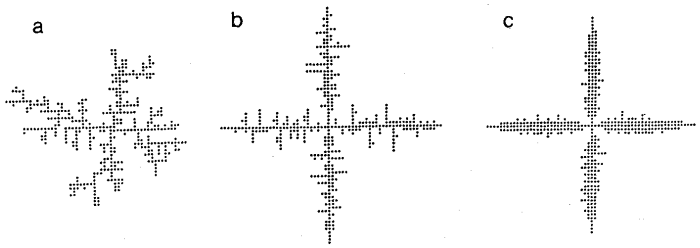

Figure 9.7. Clusters consisting of 400 particles generated on the square lattice using the noise-reduced diffusion-limited aggregation algorithm. (a) m=2, random fractal; (b) m=20, dendritic growth, and (c) m=400, noisy needle crystal (Kertész and Vicsek 1986).

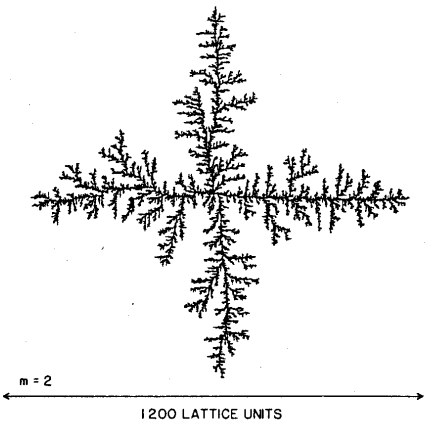

Figure 9.8. Noise-reduced diffusion-limited aggregate (m=2, N= 50,000) generated on the square lattice (Kertész *et al* 1986).

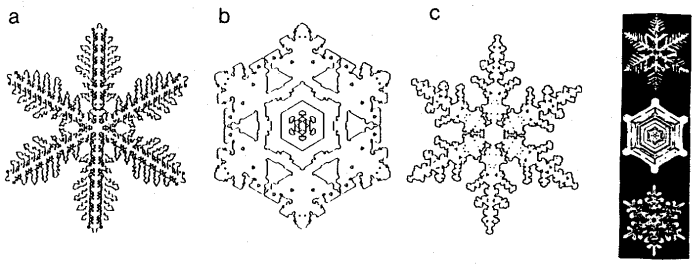

Figure 9.11. Three examples for patterns generated by the deterministic growth model on a triangular lattice. (b) and (c) were obtained by changing the parameters a and b of equation (9.13) randomly during the growth (Family *et al* 1987). The inset shows a few typical snowflakes reproduced from Bentley and Humpreys (1962).

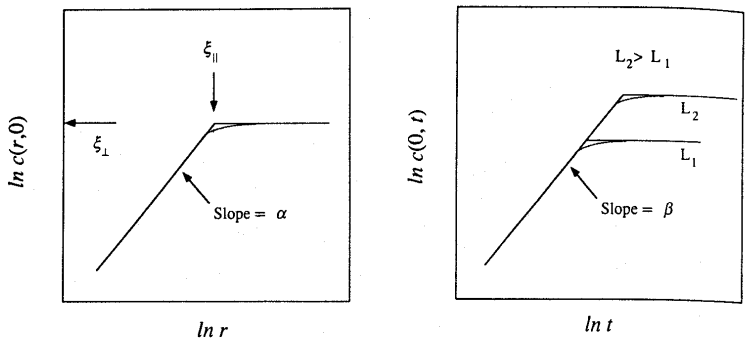

Figure 12.1. Schematic plots of the height correlation functions $c(r,0)$ and $c(0,t)$.

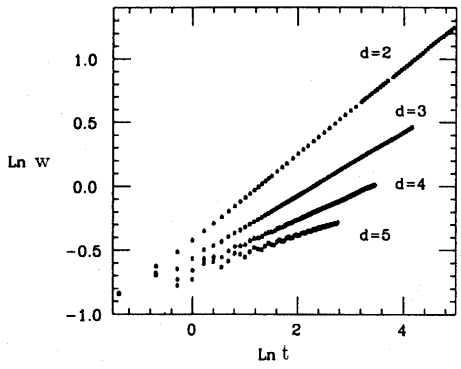

Figure 12.2. The time (average height) dependence of the width in the restricted solid-on-solid model for surfaces grown in $d = 2$ to 5 dimensions (Kim and Kosterlitz 1989). Estimates for the exponent β can be obtained from the slopes of the straight lines fitted to these data.

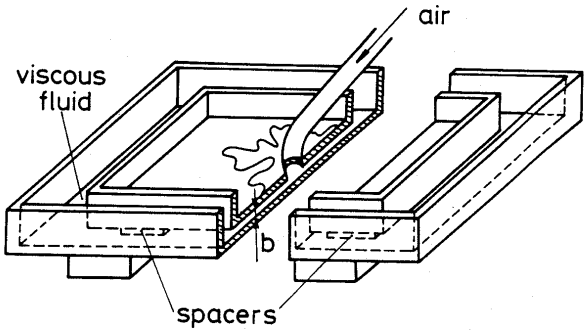

Figure B.1. Schematic picture of a radial Hele-Shaw cell. Its cross-section is also indicated. The distance between the plates is denoted by b.

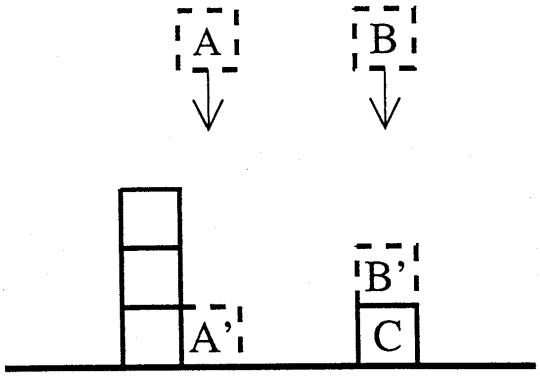

Figure 4.1: Random deposition model. Particles A and B are dropped from random positions above the surface and are deposited on the top of the column under them. In contrast to BD, in RD the height of the interface in a given point *does not depend* on the height of the neighboring columns.

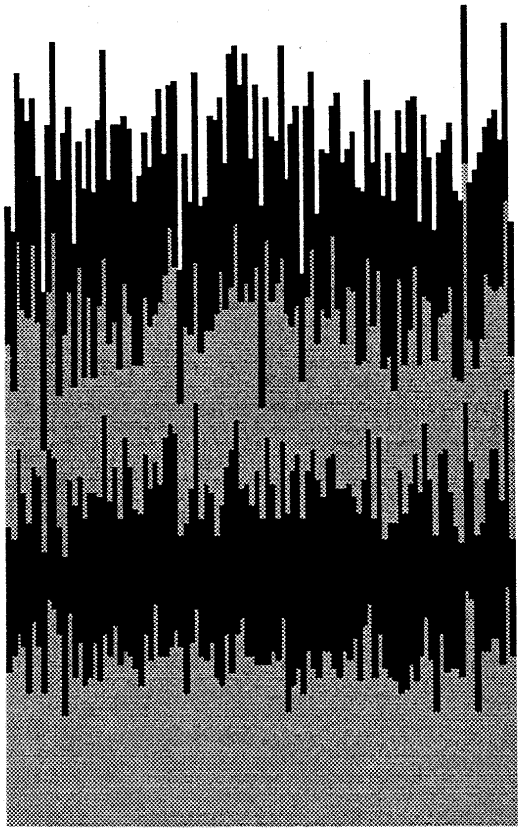

Figure 4.2: A typical interface generated by the random deposition model after depositing 16,000 particles on a substrate of size $L = 100$. The shading code reflects the arrival time of the particles: after the deposition of each set of 4000 particles, the shading changes. Note the rapid increase in the roughness and the uncorrelated nature of the surface, in contrast to the case of ballistic deposition (Fig. 2.2).

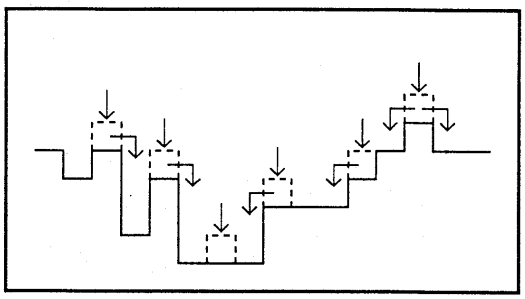

Figure 5.1: Random deposition with surface relaxation. The freshly-deposited atoms do not stick irreversibly to the site they fall on, but rather they can "relax" to a nearest neighbor if it has a lower height.

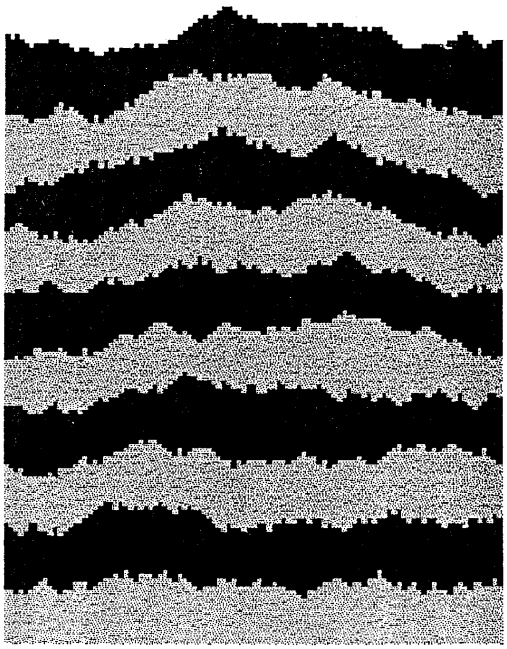

Figure 5.2: The interface at 10 successive times for a simulation of random deposition with surface relaxation, obtained by depositing 35,000 particles on a substrate of size $L = 100$. The shading reflects the arrival time of the particles: after the deposition of each set of 3500 particles, the shading changes. Note that the interface is smoother than that shown in Fig. 4.2 for the RD model.

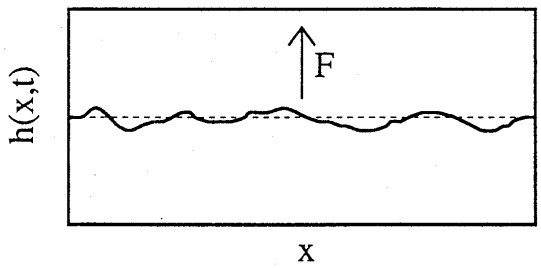

Figure 5.3: Schematic illustration of a typical one-dimensional interface $h(x,t)$ driven by an external force F, where $F = 0$ corresponds to the case of an equilibrium interface studied in this chapter. The interface is single-valued (no overhangs allowed) and has a well-defined orientation (dashed line).

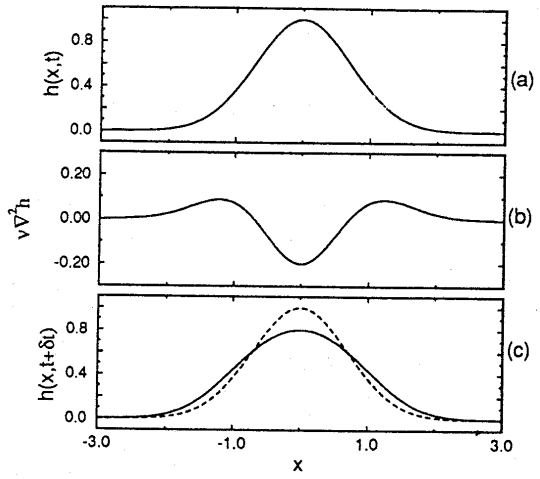

Figure 5.4: The effect of the surface tension ν in (5.6) on the morphology of the interface. Suppose that at time t the interface has a height fluctuation or "bump," as shown in (a). In (b) we show that the $\nu\nabla^2 h$ term, which is *negative* at the maximum of $h(x,t)$. At time $t+\delta t$, the height becomes, $h(x,t+\delta t) \simeq h(x,t) + \delta t \times \nu\ \nabla^2 h(x,t)$ [shown as a continuous line on (c)], where $\delta t \to 0$ and we neglect the effect of the noise $\eta(x,t)$. For comparison, we replot as a dashed line the original function $h(x,t)$. The surface tension reduces the height of the original "bump" by redistributing the surface height: material is taken from the highest point and "redistributed" on the two sides. As a result the *average* height of the interface remains unchanged. Note that (c) shows roughly what occurs in random deposition with surface relaxation in that the newly-arriving matter that created the bump is redistributed to other parts of the surface.

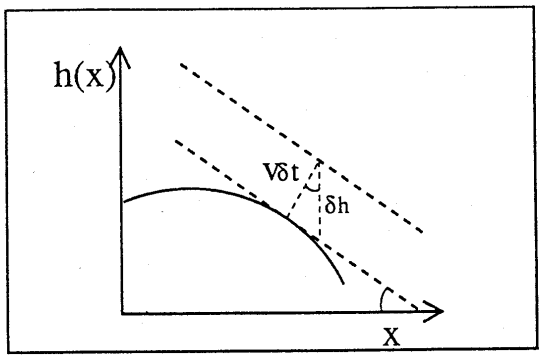

Figure 6.1: The origin of the nonlinear term in the KPZ equation (6.4). Growth occurs along the local normal v.

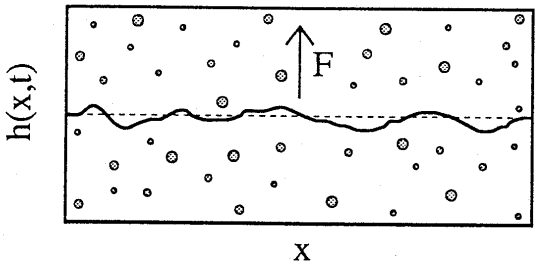

Figure 9.2: Schematic representation of an interface in random environment. The shaded circles represent randomly distributed pinning centers, whose position and pinning strength is independent of time (quenched).

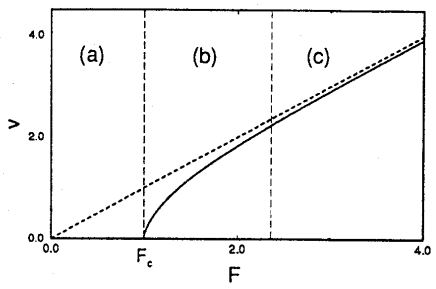

Figure 9.3: The velocity of the driven interface as a function of the driving force F. We can distinguish the three main regimes (a)-(c) on the figure. (a) For $F < F_c$ the interface velocity is zero, being pinned by the quenched randomness. (b) Near the depinning transition, for $F > F_c$, the velocity varies according to (9.3). (c) Finally, for very large driving forces, $F \gg F_c$, the velocity of the interface is proportional to the driving force. (The velocity and force units are arbitrary).

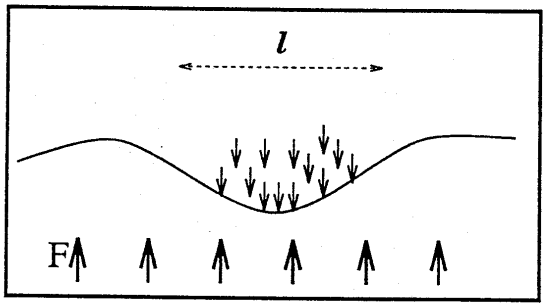

Figure 9.4: Schematic illustration of pinning of an interface portion of size ℓ. The local impurities (small arrows) oppose the motion of the interface, acting against the external driving force F and the elastic forces generated by the local curvature of the interface.

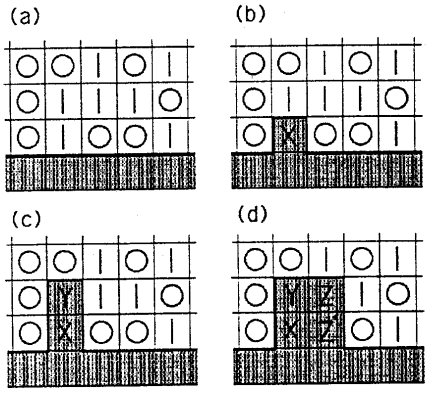

Figure 10.2: The DPD (directed percolation depinning) model for interface growth with erosion of overhangs. "Wet" cells are shaded, while dry cells are randomly blocked with probability p (indicated by O) or unblocked with probability $(1-p)$ (indicated by |). The interface between wet and dry cells are shown by a heavy line. (a) $t=0$, (b) $t=1$, (c) $t=2$ and (d) $t=3$. (After [50]).

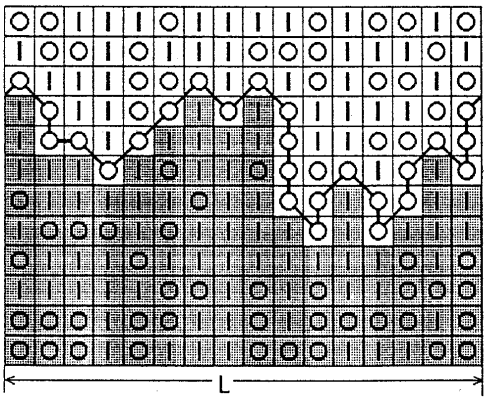

Figure 10.3: Shown as a bold line is a *spanning* path formed by connected nearest-neighbor and next-nearest-neighbor blocked cells which pin the interface. Note that various *nonspanning* clusters of blocked cells (found inside the wet region) are not sufficient to pin the interface. (After [50]).